

Hierarchical ZnO aggregates assembled by orderly aligned nanorods for dye-sensitized solar cells†

Cite this: *CrystEngComm*, 2013, 15, 1210

Dapeng Wu,^{ab} Zhiyong Gao,^{ab} Fang Xu,^a Jiuli Chang,^a Wenguang Tao,^a Jinjin He,^a Shuyan Gao^a and Kai Jiang^{*ab}

Hierarchical ZnO aggregates assembled by orderly aligned nanorods were prepared *via* a facile solvothermal method using diethylene glycol as solvent and zinc acetate dehydrate as precursor. Time dependent trails evidenced that the formation of the hierarchical aggregates experienced a multistep self-assembly process. Moreover, it was found that the reaction medium plays an important role in the assembling process and the diameter of the product could be tuned by simply altering the precursor dosage. The hierarchical product was further applied as scattering layer in bi-layered dye-sensitized solar cell (DSSC), and a high conversion efficiency of 5.2% was demonstrated, indicating a substantial improvement compared with the nanoparticle cell of 2.7%. Based on the optical and electrochemical investigations, the high conversion efficiency was mainly ascribed to the unique hierarchical structure of the ZnO aggregates. The rough surface of the nanorod subunits could enhance the dye loading capacity and the aggregates with micrometer sized diameter could improve the scattering effect. Moreover, the orderly aligned nanorods could minimize the grain boundaries, suppress the surface recombination and provide a direct pathway for fast electron transport, which therefore enhance the collection efficiency of the photoelectrons.

Received 8th September 2012,
Accepted 18th November 2012

DOI: 10.1039/c2ce26460a

www.rsc.org/crystengcomm

1. Introduction

Zinc oxide, which has a direct band gap of ~ 3.3 eV and large exciton binding energy of 60 meV, is one of the most versatile functional semiconductors. ZnO nanostructures with particularly engineered size and morphology could bring forth desirable physical and chemical properties. Especially, ZnO hierarchical structures with various assembling patterns are of great research interest because these complicated structures could ensure their prominent performances in different functional devices.^{1–4} However, different from the hierarchical structural assembled from zero dimensional nanoparticles, the great mass and volume of the primary building blocks make them difficult to assemble into orderly aligned hierarchical structures with the assistant of weak interactions such as the van der Waals and electrostatic forces.^{5–7} Generally, the assembling of the subunits is assisted with the macroscale forces from organic molecules, for example, ZnO microspheres assembled by the nanorods were fabricated with the aid of the

cross-linking function of poly(sodium 4-styrenesulfonate) and ZnO hollow microspheres were also prepared *via* a biopolymer directed crystal growth and mediated self-assembly of well aligned nanorods.^{8,9}

Dye-sensitized solar cell (DSSC) represents a new generation solar energy conversion device which have attracted much research attention in the past two decades due to their appealing qualities such as low producing cost, short energy payback time and convenience for multiple application purposes.^{10,11} ZnO was regarded as the best alternative for TiO₂ materials because of the similar electron band structure, excellent bulk electron mobility and sophisticated structural/morphological engineering strategies.^{12–17} Therefore, these unique advantages of ZnO were expected to expand the possibilities in term of designing the DSSC photoanode. To date, a vast variety of ZnO nanostructures such as nanoparticles, tetrapods, nanosheets and hierarchical aggregates were designed and fabricated for the photoanode materials.^{18–27} However, the highest PCE of ZnO based DSSCs merely reached to $\sim 7.5\%$ adopting polydisperse submicron sized hierarchical ZnO aggregates as photoanode and N719 as sensitizer, which is still far less than the PCE of the TiO₂ based DSSCs.²⁸

In order to achieve high PCE on ZnO based DSSCs, many schemes were developed to enhance the light harvesting and the charge collection efficiency. There are generally two methods to improve the harvesting of the incident light: mixing the nanoparticles film with submicron sized ZnO

^aSchool of Chemistry and Chemical Engineering, Henan Key Laboratory of Photovoltaic Materials, Xinxiang, Henan, P. R. China

^bEngineering Technology Research Center of Motive Power and Key Materials of Henan Province, Xinxiang, Henan 453007, P. R. China.
E-mail: jiangkai6898@126.com; Fax: +86 373 3326209

† Electronic supplementary information (ESI) available: XRD characterizations of the intermediate samples; SEM images of the Film-S2. See DOI: 10.1039/c2ce26460a

particles as scattering centers, and depositing additional scattering layer on the nanoparticles film.^{29–32} Nevertheless, the larger size particles inevitably reduce the overall surface area and the dye loading capacity of the film. To mediate this competition, ZnO submicron sized aggregates consisting of 10–20 nm nanocrystals were employed as dual-functional material to improve the scattering of the incident light without sacrificing the accessible surface area.^{33,34} To achieve high collection efficiency, one dimensional ZnO nanostructures are intentionally introduced to reduce the recombination rate by offering direct pathway for electron transport.^{35,36} However, these one dimensional ZnO structures usually possess limited surface area which consequently results in low short circuit current density.^{37,38} Therefore, it is of great significance to integrate the required qualities of large surface area, prominent scattering effect and high electron transport rate into the ZnO based photoanode. In addition, due to the intrinsic instability in acid ambient, the ZnO nanoparticles are vulnerable to the ruthenium based dyes. Moreover, the dyes containing complexing agents can also detach the Zn^{2+} from the host lattice to generate Zn^{2+} -dye agglomerations at the interface, resulting in low injection efficiency and high recombination rate.^{39–41} The modification of another protecting layer (like SiO_2 , Al_2O_3 , TiO_2 and ZnS) could indeed enhance the stability of ZnO surface and suppress the recombination.^{42–46} However it would inevitably bring forth injection problem and extra fabrication cost.⁴⁷ Therefore, there are still many challenges to promote the PCE of ZnO based DSSCs.

This paper reported a facile fabrication of ZnO hierarchical comprised of orderly aligned nanorods, and an interesting self-assembly process was observed by the time dependent trials. Moreover, the diameter of the products could be turned by simply altering the precursor dosage. We intentionally deposited the as-prepared hierarchical ZnO aggregates, which are assembled by orderly aligned nanorods and have different diameter ranges, on the nanoparticle film to construct the bi-layered DSSCs. Due to the promoted scattering effect and the suppressed recombination, a high PCE of 5.2% was demonstrated in the bi-layered cell, which indicated a substantial PCE enhancement compared with the cell derived from monolayer ZnO nanoparticle (2.7%).

2. Experimental section

2.1. Preparation of the ZnO hierarchical aggregates

1 g zinc acetate dehydrate ($\text{Zn}(\text{Ac})_2 \cdot 2\text{H}_2\text{O}$) was dispersed into 40 mL diethylene glycol (Aldrich, 99%). After stirring at room temperature for 1 h, the suspension was transferred into 50 mL Teflon-lined autoclave and heated at 160 °C for 6 h. The residues were thoroughly rinsed with distilled water and absolute ethanol by centrifugation. The final products were dried in vacuum for later use. For the time dependent trails, the intermediate samples were respectively collected at 0.5 h, 1 h, 2 h and 4 h to monitor the growing process. Moreover, the $\text{Zn}(\text{Ac})_2 \cdot 2\text{H}_2\text{O}$ dosage was also adjusted from 0.5 g to 1.5 g to control the size and morphology of the products, in which the

reaction time was set at 6 h and the other reaction parameters were kept unchanged.

2.2. Preparation of 20–30 nm ZnO nanoparticles

0.5 g $\text{Zn}(\text{Ac})_2 \cdot 2\text{H}_2\text{O}$ was dispersed into 40 mL absolute ethanol. After stirring for 1 h, the suspension was transferred into 50 mL Teflon-lined autoclave and heated at 160 °C for 4 h. The white powder was rinsed with distilled water and absolute ethanol, and finally dried in vacuum for later use.

2.3. Material characterizations

The products were characterized by field-emission scanning electron microscopy (FESEM, HITACHI, S4800), transmission electron microscopy (TEM, FEI Tecnai F30) equipped with a X-ray energy diffusion spectra with detection limit of 0.3–1%, X-ray powder diffraction (XRD, Rigaku D/max-2500 diffractometer with $\text{Cu K}\alpha$ radiation, $\lambda = 0.1542$ nm, 40 kV, 100 mA).

2.4. Fabrication of the DSSCs

Hydroxypropyl cellulose (Aldrich) was firstly added to diethylene glycol with a concentration of ~10 wt% to prepare the paste. To prepare the nanoparticle slurry, ~0.4 g the as-prepared paste was added into 0.2 g ZnO nanoparticles, and stirred vigorously to generate the homogeneous slurry. To prepare the scattering layer slurries, 25 wt% nanoparticles were mixed in the ZnO aggregates powders. Then, the slurries were prepared in a similar process with the nanoparticle slurry. The bi-layered films were constructed by the doctor-blade method through two-step calcination. The nanoparticle slurry was spread onto FTO glass substrate (TEC-8, LOF) with adhesive tape to control the film thickness. After drying in air, the film was heated up to 450 °C and maintained for 30 min. After calcination, the ZnO aggregates slurries were deposited on the nanoparticle layer and annealed with the same heating profile. After cooled to ~70 °C, the films were sensitized in a ethanol solution of *cis*-bis(isothiocyanato)bis(2,2'-bipyridyl-4,4'-dicarboxylate) ruthenium(II)bis-tetrabutylammonium (N719, Solaronix SA, Switzerland, 3×10^{-4} M) for 50 min. The dyed films were then sandwiched together with platinized FTO counter electrodes and the electrolyte was then injected into the cell from the edges by capillarity action. The content of the electrolyte is 0.05 M LiI, 0.03 M I_2 , 0.5 M *tert*-butylpyridine, 0.1 M GuNCS and 1 M BMII in a mixture of 85% acetonitrile and 15% valeronitrile.

2.5. Photovoltaic measurements

The photocurrent–voltage (I – V) measurements were performed on Keithley 4200 semiconductor characterization system using simulated AM 1.5 sunlight with an output power of 100 mW cm^{-2} produced by a solar simulator (Newport 69911). The incident monochromatic photo-to-electron conversion efficiency (IPCE) was recorded on a Keithley 2000 sourcemeter under the irradiation of a 150 W tungsten lamp with 1/4 m monochromator (Spectral Product DK240). The optical diffuse-reflection spectra were measured by spectrophotometer (HITACHI U-4100). The electrochemical impedance spectra (EIS) were measured in dark and at an applied negative bias voltage. The spectra were scanned at a frequency ranging from 100 kHz to 100 MHz with a computer controlled potentiostat

(EG&G, M283) equipped with a frequency response detector (EG&G, FRD100).

3. Results and discussion

3.1. Morphology and structure characterizations

Fig. 1a displays the as-prepared hierarchical ZnO aggregates which are assembled by several individual microspheres and possess a wide diameter distribution of 4–8 μm . Moreover, some individual microspheres could be also observed with smaller diameter of 1–3 μm . As depicted in Fig. 1b, a broken aggregate reveals the hierarchical structures are assembled by orderly aligned nanorods about 500 nm to 1 μm in length. In addition, the cross section (c area) and the surface (d area) of the aggregates were further magnified and shown in Fig. 1c and d. Fig. 1c shows the orderly aligned nanorods are radially assembled and have rough surface. In addition, Fig. 1d discloses the nanorods are about 10–30 nm in diameter and with typical hexagonal edges. Fig. 2 shows that the XRD diffraction peaks of the aggregates match well with the standard values (JCPDS No. 36-1451) and no impurity is detected, suggesting the product has high purity and wurtzite structure. Moreover, it is interesting to find that the full width of the (002) peak at the half-maximum is the narrowest when compared with the other diffraction peaks, inferring that the as-generated ZnO subunit was promoted along the [0001] direction to form the rod-like structures.⁴⁸

Fig. 3a shows a nanorod bundle detached from the hierarchical ZnO aggregate. The nanorods have a rough surface and are radially aligned to form a fan-shaped bundle. Moreover, the bright and narrow slits (marked in white squares) indicate there are channels existing among the rods, which may facilitate the diffusion of the N719 solution during the sensitizing. Fig. 3b and c respectively presents the HRTEM image of the b and c area marked with black squares in Fig. 3a.

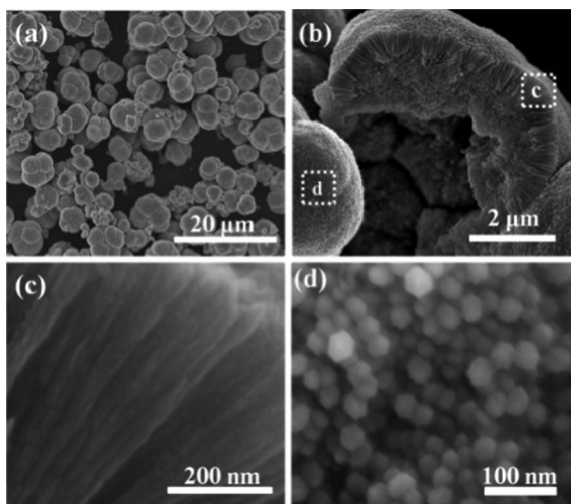


Fig. 1 SEM images of the as-prepared hierarchical ZnO aggregates with (a) low, (b) intermediate and (c, d) high magnifications.

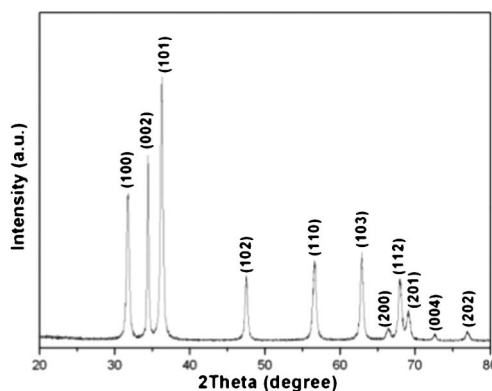


Fig. 2 XRD pattern of the as-prepared hierarchical ZnO aggregates.

Fig. 3b shows the lattice fringes are clear and the interplanar spacing is measured as 0.26 nm, indicating the ZnO nanorod is growing along the [0001] direction. Moreover, Fig. 3c indicates the surface of the nanorod is not smooth but distributed with holes about several nanometers in diameter (marked with white circles), which could improve the surface roughness and the dye loading capacity. The corresponding fast Fourier transfer (FFT) image (inset of Fig. 3a) reveals a dot like pattern, indicating the nanorod is virtually single crystal and stretching along the [0001] direction. Fig. 3d displays the EDS characterization of the nanorod bundle, in spite of the C and Cu peaks deriving from the copper grid, no impurity elements are detected, confirming the sample has high purity.

3.2. Growth mechanism and size control

In order to reveal the growth mechanism of the hierarchical ZnO aggregates, time dependent trails were carried out to monitor the grow process. After 0.5 h reaction, Fig. 4a shows the firstly generated precipitate was composed of nanoparticles and about several nanometers in diameter. As the reaction reached to 1 h, ZnO nanorods about 200–300 nm in length were formed (Fig. 4b). Moreover, at this stage, ZnO nanoparticles about 10–20 nm in diameter were found coexisting with

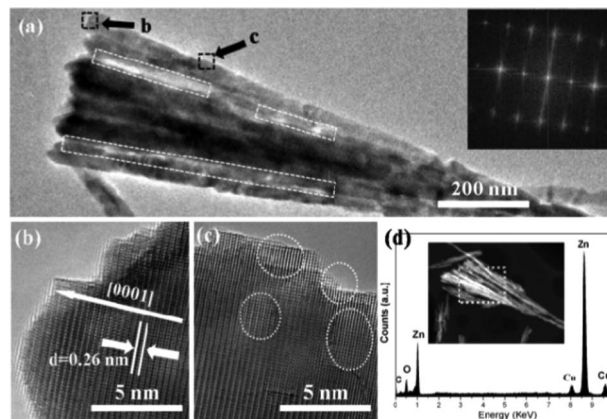


Fig. 3 (a) TEM image, (b, c) HRTEM images and (d) EDS characterization of the nanorod bundle detached from the aggregates. The inset of (a) is the FFT image.

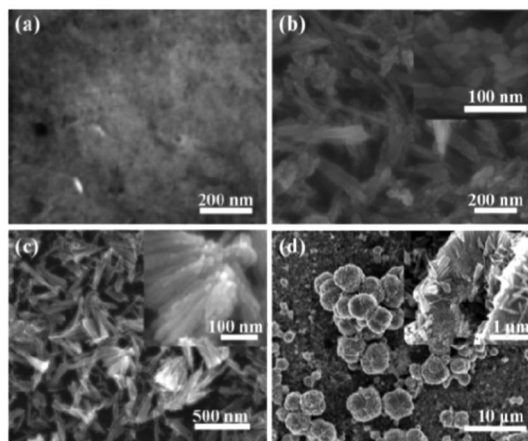
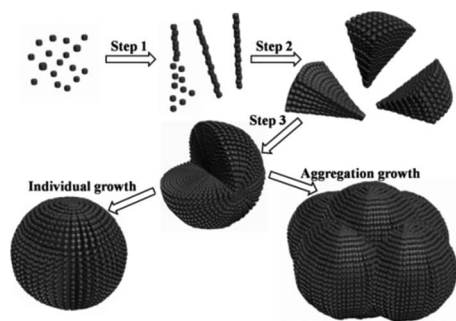


Fig. 4 SEM images of the intermediate products collected at different times: (a) 0.5 h, (b) 1 h, (c) 2 h and (d) 4 h.

the nanorods (inset of Fig. 4b). When the reaction proceeded to 2 h, nanorod bundles about 500 nm in length were observed, and the inset image indicates the bundles possess rough surface and assembled by nanoparticles (Fig. 4c). After 4 h, micrometer sized hierarchical aggregates appeared in the sample (Fig. 4d). Meanwhile, the inset image suggests many nanorod bundles are littering aside the hierarchical aggregates, indicating the bundles were not fully assembled yet. The corresponding XRD investigation (Fig. S1, ESI[†]) shows that the nanoparticles obtained at the early stage are wurtzite ZnO having poor crystal quality. In addition, the crystal quality of the intermediate ZnO products is gradually improved as increasing the reaction time.

As illustrated in Scheme 1, a multistep self-assembly mechanism is proposed to elucidate the growth of the hierarchical structures. At the initial stage, the decomposition of $\text{Zn}(\text{Ac})_2 \cdot 2\text{H}_2\text{O}$ generates the ZnO nucleus. The nonpolar diethylene glycol medium strongly inhibits the anisotropic growth of the ZnO crystals.⁴⁹ Therefore, ZnO nanoparticles are firstly formed in the reaction, and the continuous decomposing of the precursor leads to the growth of the particle size. Because of the (0001) facet of the ZnO nanoparticle, terminated by Zn atoms, is positively charged, the negatively



Scheme 1 Illustration of the multistep self-assembly growth mechanism from ZnO nanoparticles to the final hierarchical aggregates.

charged (000-1) facet of another particle is apt to link together by the electrostatic attraction. Therefore, the finally formed nanorods all stretching along the [0001] direction by means of the oriented attachment.^{50–52} As the reaction proceeded, the nanoparticles would further fuse together to generate high quality single crystal nanorods. Considering nanoparticles are the primary units for the later assembly, it is reasonable to understand that the nanorods possess rough surface. Although the reason why the orderly aligned nanorod bundles all taking radial assembling pattern remains a mystery, the driving force may also attribute to the minimization of the system free energy (Step 2).⁵³ Subsequently, considering the nanorods are radially aligned to develop the fanshaped bundles, it is reasonable to anticipate that the later assembled products should exhibit spherical shapes (Step 3). As depicted in Scheme 1, the individual growth of the spherical product leads to the formation of individual microspheres. Meanwhile, the aggregation growth results in large size aggregates containing several microspheres. The aggregation growth may further improve the connectivity among the individual microspheres and lead to a better electron transport.

In addition, as displayed in Fig. 5, the nonpolar diethylene glycol medium is found to exert great importance for the self-assembly process. In order to eliminate the effect of the crystal water contained in the precursor, the $\text{Zn}(\text{Ac})_2 \cdot 2\text{H}_2\text{O}$ was firstly dehydrated under 100 °C for 2 h before transferred into the solvothermal reaction system. After 6 h, the diameter of the as-obtained aggregates is generally reduced to less than 2 μm (Fig. 5a). The inset shows the aggregate comprises of nanoparticles about 10–20 nm in diameter, which is different from nanorod subunits with hexagonal cross-section. As 0.5 mL water was introduced to the reaction, although the morphology of the product is slightly changed, many small particles are formed beside the aggregates (Fig. 5b). If the water dosage was further elevated to 1 mL, the assembling process is obviously jeopardized and only several individual aggregates survive. Moreover, the diameter of the subunit increased to 30–100 nm as shown in the inset (Fig. 5c). The assembling was totally destroyed and no aggregate was formed

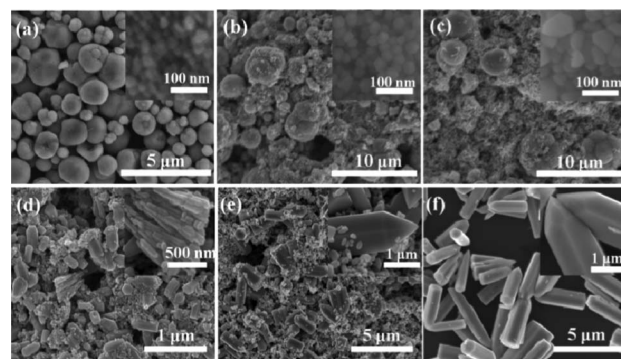


Fig. 5 SEM images of the products prepared with different water/diethylene glycol ratios (volume/volume (mL)): (a) 0 : 40 (the $\text{Zn}(\text{Ac})_2 \cdot 2\text{H}_2\text{O}$ was dehydrated under 100 °C for 2 h prior to the solvothermal reaction), (b) 0.5 : 39.5, (c) 1 : 39, (d) 2 : 38, (e) 10 : 30 and (f) 40 : 0. The insets represent the magnified images.

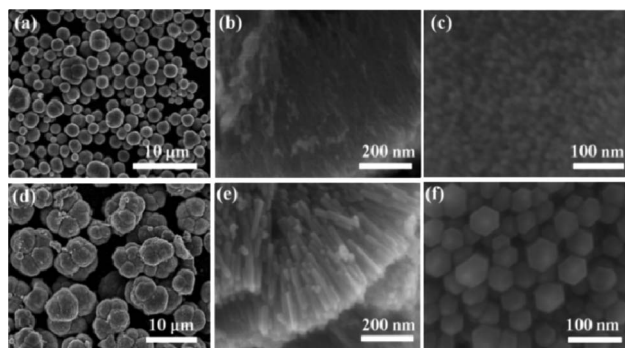


Fig. 6 SEM images of the hierarchical ZnO aggregates prepared with different $\text{Zn}(\text{Ac})_2 \cdot 2\text{H}_2\text{O}$ dosages of (a–c) 0.5 g and (d–f) 1.5 g.

when 2 mL water was introduced to the reaction system (Fig. 5d). Moreover, if the water dosage was further increased, micrometer sized ZnO rods with sharp tips and hexagonal cross-sections were formed, indicating the anisotropic growth was recovered in the solvent with high polarity (Fig. 5e and f). Therefore, in spite of the function to suppress the anisotropic growth of the ZnO crystal, the diethylene glycol reaction system could also stabilize the intermediate products (nanoparticles, nanorods and the rod bundles) and prevent them from irregularly aggregating probably due to its high viscosity, which leads to the highly ordered assembling of the subunits and finally shape the hierarchical ZnO aggregates composing of orderly aligned nanorods.

Fig. 6 a–c represent the SEM images of the sample prepared with 0.5 g $\text{Zn}(\text{Ac})_2 \cdot 2\text{H}_2\text{O}$ dosage. Fig. 6a shows that except for several large size aggregates, the sample mainly consists of individual microspheres about 2 μm in diameter. Fig. 6b displays the cross section view of a broken microsphere, suggesting the product is assembled by radially aligned nanorods with very thin diameters. The surface view in Fig. 6c indicates the orderly assembled nanorods are ~ 10 nm in diameter. Fig. 6d–f display the product obtained with 1.5 g $\text{Zn}(\text{Ac})_2 \cdot 2\text{H}_2\text{O}$ dosage. It is reasonable to understand that with increasing precursor dosage, the sample mainly consists of hierarchical aggregates containing several microspheres, and the diameters are increased to 8–10 μm . The cross section view displayed in Fig. 6e shows the orderly aligned nanorods possess smooth surface. The surface view in Fig. 6f confirms that the diameter of the nanorods increases to 30–60 nm. Moreover, the perfect hexagonal cross sections of the nanorods suggest the crystal quality is further improved.

3.3. Photovoltaic performances

In order to investigate the photovoltaic performances of the as-prepared hierarchical ZnO aggregates, we compared four cells with different film structures. The cell derived from a monolayer of ZnO nanoparticles ($\sim 16 \mu\text{m}$) is labeled as Cell-NP. The hierarchical ZnO samples prepared with $\text{Zn}(\text{Ac})_2 \cdot 2\text{H}_2\text{O}$ dosage of 0.5, 1 and 1.5 g are respectively deposited as scatter layers ($\sim 10 \mu\text{m}$) on ZnO nanoparticle films ($\sim 6 \mu\text{m}$) to construct the bi-layered cells and denoted as Cell-S1, Cell-S2 and Cell-S3. The photoanode structures of Cell-S2 are displayed in Fig. S2, ESI,† The cross section view depicted in Fig. S2a, ESI,† shows the underlayer is closely packed with nanoparticles and the overlayer is composed of both large size hierarchical aggregates and nanoparticles which are intentionally mixed to improve the connectivity among the individual aggregates. Fig. S2b, ESI,† shows the surface of the scattering layer, it is found that the gaps among the aggregates are filled with nanoparticles to allow better connectivity. Fig. S2c, ESI,† proves the nanoparticles in the underlayer are generally 20–30 nm in diameter. Moreover, the dye loading capacity of the films was evaluated by desorbing the dyed films in 0.5 M NaOH aqueous solution (Table 1). The capacity of Cell-NP is determined as $2.4 \times 10^{-7} \text{ mol cm}^{-2}$, while Cell-S1 and Cell-S2 have the similar capacity of 2.1 and $2.0 \times 10^{-7} \text{ mol cm}^{-2}$, respectively. The nanorod subunits of the sample prepared with 1.5 g $\text{Zn}(\text{Ac})_2 \cdot 2\text{H}_2\text{O}$ dosage possess large diameter and smooth surface which results in low surface area. Therefore, Cell-S3 exhibits the lowest dye loading capacity of $1.7 \times 10^{-7} \text{ mol cm}^{-2}$.

Fig. 7 shows the photocurrent–voltage (I – V) curves of the DSSCs and the detailed photovoltaic characteristics are displayed in Table 1. Considering the open circuit voltage (V_{oc}) varies little among the four cells, the PCE variation is mainly attributed to the change in the filling factor (FF) and the short circuit current (J_{sc}). Conspicuously, the bi-layered DSSCs give much higher FF than that of the Cell-NP, which leads to prominent PCE improvements compared with the monolayer nanoparticle cell. Typically, Cell-S2 demonstrates a J_{sc} of 13.5 mA cm^{-2} , V_{oc} of 614 mV, and FF of 62.7%. As a result, the PCE reaches up to 5.2%, indicating a significant improvement compared with Cell-NP (2.7%).

Fig. 8 depicts the UV-Vis reflection spectra of the single layer films composed of ZnO nanoparticles and hierarchical ZnO aggregates prepared under different precursor dosages (mixed with 25 wt% nanoparticles). With similar film thickness of $\sim 10 \mu\text{m}$, the nanoparticle film exhibits high transparency, especially at the region of 600–800 nm. On the other hand, the films derived from the hierarchical aggregates all possess high reflectance, which could improve the scattering of the incident

Table 1 Photovoltaic performance of DSSCs (the active area for all the cells are about $\sim 0.16 \text{ cm}^2$)

Cells	J_{sc} (mA cm^{-2})	V_{oc} (mV)	FF (%)	PCE (%)	Dye absorption (mol cm^{-2})
Cell-NP	8.9	614	49.4	2.7	2.4×10^{-7}
Cell-S1	11.7	586	63.0	4.3	2.1×10^{-7}
Cell-S2	13.5	614	62.7	5.2	2.0×10^{-7}
Cell-S3	12.6	596	61.6	4.6	1.7×10^{-7}

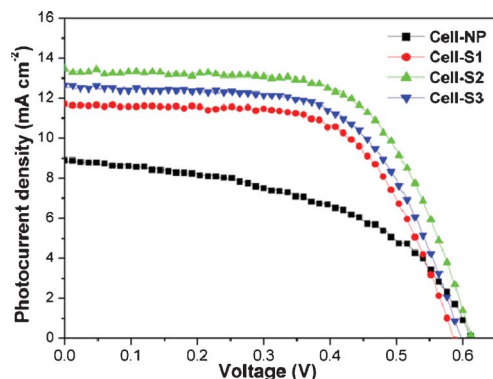


Fig. 7 I - V curves of the DSSCs measured under one sun illumination (AM 1.5G, 100 mW cm^{-2}).

light. Moreover, based on previous reports, the scattering effect of the particles is size dependent.^{54,55} The polydisperse particles usually have better scattering effect compared with the monodisperse ones because they could induce scattering enhancement in a wider wavelength range.³²

Fig. 9 shows the incident photon-to-current conversion efficiency (IPCE) spectra as a function of wavelength for the DSSCs. The bi-layered cells all exhibit higher IPCE value. Particularly, compared with Cell-NP, clear IPCE peaks are observed in Cell-S1, Cell-S2, and Cell-S3 at the range from 500 nm to 700 nm, which derives from the improved scattering effect. Moreover, considering the nanorods with rough surface could increase the dye loading amount, Cell-S2 has the highest absolute IPCE value in the entire wavelength region, which is in agreement with its high J_{sc} . As mentioned above, the acid dye solution could impact the surface integrity of the small size ZnO particles, resulting in low injection rate and high electron recombination.^{56,57} Therefore, although Cell-NP has high dye loading amount, it shows the lowest IPCE value. Similarly, Cell-S1 derives from the aggregates assembled by thin nanorods which are also vulnerable to the acid dye solution. Therefore, it exhibits a relative low IPCE value among

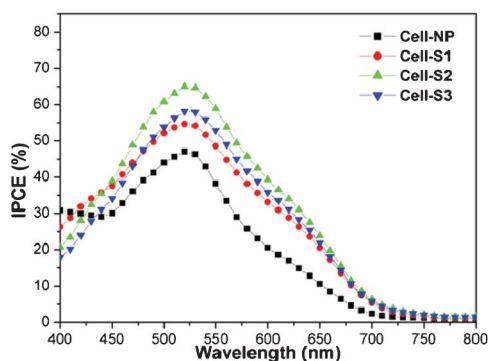


Fig. 8 The UV-Vis reflection spectra of the single layer films composed of 20–30 nm ZnO nanoparticles, and the ZnO hierarchical aggregates prepared with $\text{Zn}(\text{Ac})_2 \cdot 2\text{H}_2\text{O}$ dosages of 0.5, 1 and 1.5 g.

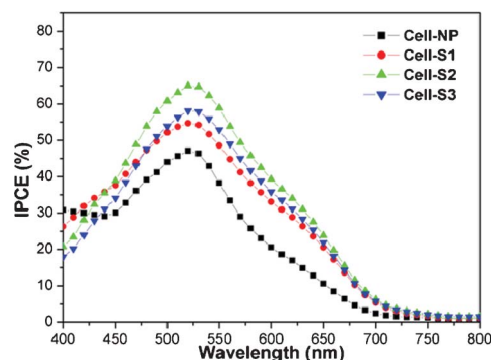


Fig. 9 Incident photon-to-current conversion efficiency (IPCE) spectra for the as-prepared DSSCs.

the bi-layered DSSCs, which could be also ascribed to the reduced injection and collection efficiency.

In order to interpret the electron recombination dynamics, the cells were tested by electrochemical impedance spectra (EIS). The measurements were performed in dark at different applied negative bias voltage.⁵⁸ Fig. 10a shows the Nyquist plots of Cell-NP and Cell-S2 measured at an applied voltage of -0.6 V . Three typical semicircles appear from high to low frequency are corresponded to the charge transfer at the counter electrode, the electron transport and the recombination at the ZnO-dye-electrolyte interface and the Nernstian diffusion in the electrolyte, respectively.^{59,60} The equivalent circuit used to fit the series resistance of R_s , charge recombination resistance of R_{ct} and the chemical potential of C is presented in Fig. 10a. The major concern of the current research is the recombination (R_{ct2}) occurring at the ZnO-dye-electrolyte interface. The as-fitted data plots of R_{ct2} and C_2 are plotted in function of the applied negative bias voltage and displayed in Fig. 10b and c. It is obvious that Cell-S2 has

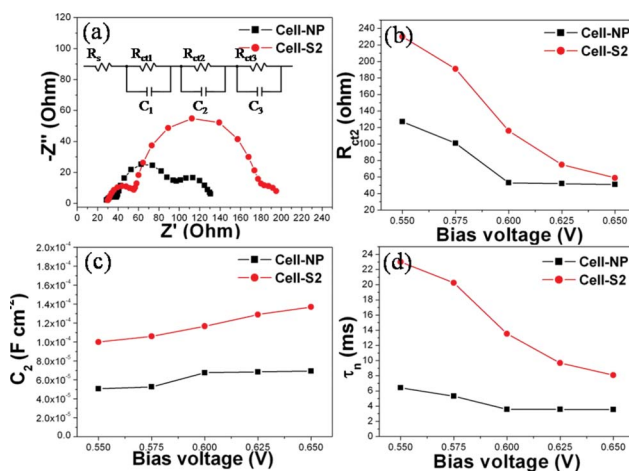


Fig. 10 Electrochemical impedance characterizations of Cell-NP and Cell-S2: (a) the Nyquist plots of the EIS data measured at -0.6 V . (b) The charge recombination resistance (R_{ct2}), (c) chemical potential (C_2) and (d) electron recombination life time (τ_n) of the cells measured at different applied negative bias voltages. The inset of (a) is the equivalent circuit.

higher R_{ct2} value than Cell-NP suggesting its advantages to retard the charge recombinations. It is understandable that the high quality and orderly aligned nanorods could not only resist the surface etching in the acid dye but also provide a direct pathway to facilitate the electron transport. Moreover, Cell-S2 possesses higher C_2 values, indicating it could efficiently accumulate the charges and enhance the charge density for a higher J_{sc} compared with that of Cell-NP.^{61,62} In addition, the electron recombination life times (τ_n) could be calculated by $\tau_n = R_{ct2} \times C_2$.⁶³ As displayed in Fig. 10d, Cell-S2 has longer τ_n at the whole voltage range than Cell-NP. For example, at the bias voltage roughly equals to the V_{oc} of the cells (-0.6 V), Cell-S2 shows a τ_n of ~ 14 ms which triples the value of Cell-NP (~ 4 ms). The prolonged τ_n could allow more effective electron transport and leads to a higher conversion efficiency of Cell-S2.

4. Conclusions

We have prepared hierarchical ZnO aggregates assembled by orderly aligned nanorods. A multistep self-assembly mechanism was proposed to elucidate the growth process of the products. Moreover, the size of the product could be tuned by simply altering the $Zn(Ac)_2 \cdot 2H_2O$ dosage. The aggregates were further used as the scattering layer in DSSC applications. The bi-layered DSSC demonstrated a high PCE of 5.2%, in contrast to the monolayer nanoparticles cell of 2.7%. The PCE enhancements could be attributed to (a) the nanorods with rough surface could increase the dye loading capacity and (b) the micrometer sized aggregates could enhance the scattering effect, which improves the harvesting of the incident light. Moreover, (c) the orderly aligned nanorods with high crystal quality could suppress the surface recombination and offer direct pathway for electron transport.

Acknowledgements

This work is supported by National Natural Science Foundation of China (61204078 and 61176004), Basic and Frontier Research Programs of Henan Province (No. 092300410240 and No. 112300410094), Natural Science Foundation of Education Department of Henan Province (2010 B150012, 2011A150017).

References

- X. D. Wang, J. H. Song, J. Liu and Z. L. Wang, *Science*, 2007, **316**, 102.
- M. H. Huang, S. Mao, H. Feick, H. Q. Yan, Y. Y. Wu, H. Kind, E. Weber, R. Russo and P. D. Yang, *Science*, 2001, **292**, 1897.
- D. P. Lyvers, J. M. Moon, A. V. Kildishev, V. M. Shalaev and A. Wei, *ACS Nano*, 2008, **2**, 2569.
- H. M. Zhang, P. R. Liu, X. L. Liu, S. Q. Zhang, X. D. Yao, T. C. An, R. Amal and H. J. Zhao, *Langmuir*, 2010, **26**, 11226.
- P. Hu, X. Zhang, N. Han, W. Xiang, Y. Cao and F. Yuan, *Cryst. Growth Des.*, 2011, **11**, 1520.
- T. Zhai, S. Xie, Y. Zhao, X. Sun, X. Lu, M. Yu, M. Xu, F. Xiao and Y. Tong, *CrystEngComm*, 2012, **14**, 1850.
- S. Ran, Y. Zhu, H. Huang, B. Liang, J. Xu, B. Liu, J. Zhang, Z. Xie, Z. Wang, J. Ye, D. Chen and G. Shen, *CrystEngComm*, 2012, **14**, 3063.
- M. Mo, J. C. Yu, L. Zhang and S. A. Li, *Adv. Mater.*, 2005, **17**, 756.
- S. Gao, H. Zhang, X. Wang, R. Deng, D. Sun and G. Zheng, *J. Phys. Chem. B*, 2006, **110**, 15847.
- B. Oregan and M. Gratzel, *Nature*, 1991, **353**, 737.
- M. Gratzel, *Nature*, 2001, **414**, 338.
- E. M. Kaidashew, M. Lorenz, H. von Wenckstern, A. H. Rahm, C. Semmelhack, K. H. Han, G. Benndorf, C. Bundesman, H. Hochmuth and M. Grundmann, *Appl. Phys. Lett.*, 2003, **82**, 3901.
- J. Halme, P. Vahermaa, K. Miettunen and P. Lund, *Adv. Mater.*, 2010, **22**, E210.
- C. Klingshirn, *ChemPhysChem*, 2007, **8**, 782.
- F. Xu and L. Sun, *Energy Environ. Sci.*, 2011, **4**, 818.
- H. Zhang, R. Wu, Z. Chen, G. Liu, Z. Zhang and Z. Jiao, *CrystEngComm*, 2012, **14**, 1775.
- L. Xu, Z. Li, Q. Cai, H. Wang, H. Gao, W. Lv and J. Liu, *CrystEngComm*, 2010, **12**, 2166.
- H. Lu, S. Wang, L. Zhao, J. Li, B. Dong and Z. Xu, *J. Mater. Chem.*, 2011, **21**, 4228.
- M. Saito and S. Fujihara, *Energy Environ. Sci.*, 2008, **1**, 280.
- W. Chen, Y. Qiu, Y. Zhong, K. S. Wong and S. Yang, *J. Phys. Chem. A*, 2010, **114**, 3127.
- Z. Li, Y. Zhou, G. Xue, T. Yu, J. Liu and Z. Zou, *J. Mater. Chem.*, 2012, **22**, 14341.
- Y. Qiu, W. Chen and S. Yang, *J. Mater. Chem.*, 2010, **20**, 1001.
- J. Lin, C. Lee and K. Ho, *J. Mater. Chem.*, 2012, **22**, 1270.
- Q. Xie, J. Li, Q. Tian and R. Shi, *J. Mater. Chem.*, 2012, **22**, 13541.
- Q. Zhang and G. Cao, *J. Mater. Chem.*, 2011, **21**, 6769.
- Y. Sun, L. Wang, X. Yu and K. Chen, *CrystEngComm*, 2012, **14**, 3199.
- H. Chen, D. Kuang and C. Su, *J. Mater. Chem.*, 2012, **22**, 15475.
- N. Memarian, I. Concina, A. Braga, S. M. Rozati, A. Vomiero and G. Sberveglieri, *Angew. Chem., Int. Ed.*, 2011, **50**, 12321.
- Y. Qiu, W. Chen and S. Yang, *Angew. Chem., Int. Ed.*, 2010, **49**, 4649.
- Y. Z. Zheng, X. Tao, L. X. Wang, H. Xu, Q. Hou, W. L. Zhou and J. F. Chen, *Chem. Mater.*, 2010, **22**, 928.
- T. P. Chou, Q. F. Zhang, G. E. Fryxell and G. Z. Cao, *Adv. Mater.*, 2007, **19**, 2588.
- Y. Zheng, J. Zhao, H. Zhang, J. Chen, W. Zhou and X. Tao, *Chem. Commun.*, 2011, **47**, 11519.
- Q. Zhang, T. P. Chou, B. Russo, S. A. Jenekhe and G. Z. Cao, *Angew. Chem., Int. Ed.*, 2008, **47**, 2402.
- Q. Zhang, T. P. Chou, B. Russo, S. A. Jenekhe and G. Z. Cao, *Adv. Funct. Mater.*, 2008, **18**, 1654.
- Y. J. Lee, D. S. Ruby, D. W. Peters, B. B. McKenzie and J. W. P. Hsu, *Nano Lett.*, 2008, **8**, 1501.
- K. Wang, J. J. Chen, W. L. Zhou, Y. Zhang, Y. F. Yan, J. Pern and A. Mascarenhas, *Adv. Mater.*, 2008, **20**, 3248.
- C. Wu and J. Wu, *J. Mater. Chem.*, 2011, **21**, 13605.

- 38 C. Wu, W. Liao and J. Wu, *J. Mater. Chem.*, 2011, **21**, 2871.
- 39 H. Horiuchi, R. Katoh, K. Hara, M. Yanagida, S. Murata, H. Arakawa and M. Tachiya, *J. Phys. Chem. B*, 2003, **107**, 2570.
- 40 N. A. Anderson, X. Ai and T. Q. Lian, *J. Phys. Chem. B*, 2003, **107**, 14414.
- 41 J. B. Asbury, N. A. Anderson, E. C. Hao, X. Ai and T. Q. Lian, *J. Phys. Chem. B*, 2003, **107**, 7376.
- 42 Y. J. Shin, J. H. Lee, J. H. Park and N. G. Park, *Chem. Lett.*, 2007, **36**, 1506.
- 43 V. Ganapathy, B. Karunagaran and S. Rhee, *J. Power Sources*, 2010, **195**, 5138.
- 44 D. Wu, Z. Gao, F. Xu, Z. Shi, W. Tao and K. Jiang, *CrystEngComm*, 2012, **14**, 7934.
- 45 M. Law, L. E. Greene, A. Radenovic, T. Kuykendall, J. Liphardt and P. D. Yang, *J. Phys. Chem. B*, 2006, **110**, 22652.
- 46 J. Qiu, M. Guo and X. Wang, *ACS Appl. Mater. Interfaces*, 2011, **3**, 2358.
- 47 Q. Zhang, B. B. Garcia, X. Zhou, Y. H. Jeong and G. Cao, *Adv. Mater.*, 2010, **22**, 2329.
- 48 U. Maiti, S. Maiti and K. Chattopadhyay, *CrystEngComm*, 2012, **14**, 640.
- 49 D. Jezequel, J. Guenot, N. Jouini and F. Fievet, *J. Mater. Res.*, 1995, **10**, 77.
- 50 Q. Zhang, S. Liu and S. Yu, *J. Mater. Chem.*, 2009, **19**, 191.
- 51 L. Zhang, L. Yin, C. Wang, N. Lun and Y. Qi, *ACS Appl. Mater. Interfaces*, 2010, **2**, 1769.
- 52 C. Pacholski, A. Kornowski and H. Weller, *Angew. Chem., Int. Ed.*, 2002, **41**, 1188.
- 53 D. Zhang, L. Sun, J. Zhang, Z. Yan and C. H. Yan, *Cryst. Growth Des.*, 2008, **8**, 3609.
- 54 D. Wu, F. Zhu, J. Li, H. Dong, Q. Li, K. Jiang and D. Xu, *J. Mater. Chem.*, 2012, **22**, 11665.
- 55 I. Yu, Y. Kim, H. Kim, C. Lee and W. I. Lee, *J. Mater. Chem.*, 2011, **21**, 532.
- 56 T. Chou, Q. Zhang and G. Cao, *J. Phys. Chem. C*, 2007, **111**, 18804.
- 57 K. Keis, J. Lindgren, S. Lindquist and A. Hagfeldt, *Langmuir*, 2000, **16**, 4688.
- 58 K. Park, J. Xi, Q. Zhang and G. Cao, *J. Phys. Chem. C*, 2011, **115**, 20992.
- 59 Q. Wang, S. Ito, M. Gratzel, F. Fabregat-Santiago, I. Mora-Sero, J. Bisquert, T. Bessho and H. Imai, *J. Phys. Chem. B*, 2006, **110**, 25210.
- 60 J. Bisquert, *J. Phys. Chem. B*, 2002, **106**, 325.
- 61 L. De Marco, M. Manca, R. Buonsanti, R. Giannuzzi, F. Malara, P. Pareo, L. Martiradonna, N. M. Giancaspro, P. Cozzolibe and D. G. Gigli, *J. Mater. Chem.*, 2011, **21**, 13371.
- 62 X. Chen, T. Ling and X. Du, *Nanoscale*, 2012, **4**, 5602.
- 63 J. Bisquert, A. Zaban, M. Greenshtein and I. Mora-Sero, *J. Am. Chem. Soc.*, 2004, **126**, 13550.